
Can the relativistic light bending model explain X-ray spectral variations of Seyfert galaxies?

Misaki Mizumoto^{1,2}, Kotaro Moriyama³, Ken Ebisawa^{1,2}, Shin Mineshige³,
Norita Kawanaka^{3,4}, & Masahiro Tsujimoto¹

¹Institute of Space and Astronautical Science (ISAS), Japan Aerospace Exploration Agency (JAXA), 3-1-1 Yoshinodai, Chuo-ku, Sagami-hara, Kanagawa, 252-5210, Japan

²Department of Astronomy, Graduate School of Science, The University of Tokyo, 7-3-1 Hongo, Bunkyo-ku, Tokyo, 113-0033, Japan

³Department of Astronomy, Kyoto University, Kitashirakawa-oiwake-cho, Sakyo-ku, Kyoto, 606-8502, Japan

⁴Hakubi Center for Advanced Research, Kyoto University, Yoshida-hommachi, Sakyo-ku, Kyoto, 606-8501, Japan

*E-mail: mizumoto@astro.isas.jaxa.jp

Received (reception date); Accepted (acceptation date)

Abstract

Many Seyfert galaxies are known to exhibit Fe-K broad emission line features in their X-ray energy spectra. The observed lines have three distinct features; (1) the line profiles are skewed and show significant low-energy tails, (2) the Fe-K band have low variability, which produces a broad and deep dip in the root-mean-square (rms) spectra, and (3) photons in this band have time lags behind those in the adjacent energy bands with amplitudes of several R_g/c , where R_g is the gravitational radius. The “relativistic light bending model” is proposed to explain these observed features, where a compact X-ray source (lamp post) above an extreme Kerr black hole illuminates the innermost area of the accretion disc. In this paper, we critically examine the relativistic light bending model by computing the rms spectra and the lag features using a ray-tracing technique, when a lamp post moves vertically on the black hole spin axis. As a result, we found that the observed deep rms dip requires that the iron is extremely overabundant ($\gtrsim 10$ solar), whereas the observed lag amplitude is consistent with the normal iron abundance. Furthermore, disappearance of the lag in the high-flux state requires a source height as high as $\sim 40 R_g$, which contradicts the relativistically broad emission line feature. Our simulations agree with the data that the reverberation feature moves to lower frequencies with larger source height, however, if this scenario is correct, the simulations predict detection of a clear Fe-K lag at low frequencies, which is not constrained in the data. Therefore, we conclude that the relativistic light bending model may not explain the characteristic Fe-K spectral variations in Seyfert galaxies.

Key words: galaxies: active — galaxies: Seyfert — galaxies: individual: IRAS 13224–3809 — X-rays: galaxies

1 Introduction

Many Seyfert galaxies are known to show a “broad iron emission line feature” in their X-ray spectra around ~ 7 keV (e.g.,

Tanaka et al. 1995). When photons are scattered in neutral materials, such as outer part of the accretion disc or the dusty torus, a sharp Fe-K fluorescent line is produced at 6.4 keV. However,

the observed iron line is commonly more broadened, often with a significant low-energy tail down to ~ 4 keV. If this feature is a real emission line, it should be skewed by some physical mechanisms; for example, Fabian et al. (1989) and Laor (1991) argued that the line broadening is caused by the gravitational redshift due to the scattering on the disc very close to the central black hole (BH). On the other hand, this spectral feature may be produced due to absorption features (e.g., Tanaka et al. 2004; Mizumoto et al. 2014; Hagino et al. 2016) or multi-continua (Noda et al. 2011), depending on different continuum models. These different mechanisms can equally explain the time-averaged spectral feature at an accuracy of the contemporary instruments, and thus origin of the broad iron line feature has still been under discussion.

Time-variability in the iron energy band should bring us key information to disentangle degenerate theoretical models. Today, two major observational clues of time variability are reported: root-mean-square (rms) spectra and time-lags. First, the rms spectra (energy dependence of the fractional variation) of Seyfert galaxies are known to have a deep and broad dip at $\sim 4 - 7$ keV (e.g., Matsumoto et al. 2003; Iso et al. 2016; Terashima et al. 2009). Namely, the Fe-K band in Seyfert galaxies have low variability compared to the continuum flux. Depth of the dip is as large as $\sim 50\%$ relative to the reference energy band of ~ 2 keV, red which is much larger than those expected solely due to the invariable and narrow neutral iron lines (e.g., Terashima et al. 2009). Second, photons in the Fe-K energy band are found to be delayed after those in the adjacent energy bands. For example, Zoghbi et al. (2012) and Kara et al. (2013b) found that the photons in 5–7 keV lag behind those in the adjacent energy bands in NGC 4151 and 1H 0707–495, respectively. The lag amplitude corresponds to several R_g/c , where $R_g = GM_{\text{BH}}/c^2$ is the gravitational radius and M_{BH} is the BH mass. The broad feature is also seen in the lag-energy spectrum. Kara et al. (2016) systematically investigated time lags of Seyfert galaxies in the *XMM-Newton* archive data, and found that $\sim 50\%$ of sources have the Fe-K reverberation lags. The lag amplitudes are commonly $1 - 9 R_g/c$, and the characteristic Fourier frequency is $\sim c/100 R_g$ Hz.

The “relativistic light bending model” has been studied extensively to explain these observational facts. In this model, relativistically-blurred reflection occurs at the innermost disc region around a Kerr BH with an almost maximum spin parameter (e.g., Fabian et al. 2002). When primary photons are scattered at the innermost region ($R \sim 1.24 R_g$), strong gravitational redshift affects the reflected spectrum, and the Fe-K fluorescent line is skewed. This model often assumes a compact corona ($\lesssim 1 R_g$), which is called as a “lamp post”, located just above the central BH with the source height of $h_s \lesssim 10 R_g$ illuminating the innermost region of the disc (e.g., Fabian & Vaughan 2003; Fabian et al. 2009). In order to explain the

rms dips, Miniutti et al. (2003) and Miniutti & Fabian (2004) considered a lamp post moving along the rotation axis. When the source height is smaller, primary photons with a power-law spectrum are less likely to escape from the strong gravitational field in the vicinity of the BH while more likely to be trapped, so the power-law component (PLC) becomes fainter. On the other hand, the reflection-dominated component (RDC) keeps almost invariant with a smaller h_s , because larger parts of the bending photons fall into the BH itself and cannot reach the disc surface. In this manner, variations of PLC and RDC are totally different, and the variability amplitudes are expected to be reduced in the Fe-K energy band where RDC is dominant. In addition, the light-travel time from the lamp post to the accretion disc is about several R_g (e.g., Kara et al. 2013b; Cackett et al. 2014). Therefore, the reverberation lags with short amplitudes ($\lesssim 10 R_g/c$) are expected.

Here, we point out potential problems in the relativistic light bending model. One problem is that the rms spectra and lags seem to require different iron abundances. The iron overabundance (3 – 20 solar) is commonly needed to explain the line profile and the rms spectra in the relativistic light bending model (e.g., Fabian et al. 2002; Chiang et al. 2015). On the other hand, numerical simulations suggest that the solar iron abundance is sufficient to explain the observed lags (Emmanoulopoulos et al. 2014; Cackett et al. 2014). Moreover, some argued that the observed deep rms dips cannot be fully explained only by the relativistic light bending model (Inoue & Matsumoto 2003; Życki et al. 2010). If the relativistic light bending model is inconsistent, we may not trust physical parameters derived by this model. For example, many papers publish a spin parameter, one of the three key parameters to characterise BHs, using this model via spectral fitting. Therefore, it is very important to investigate validity of the relativistic light bending model.

In the previous studies, the two features about time variability in the Fe-K band, rms dips and reverberation lags, were explained individually, not simultaneously. Therefore, in this paper, we perform a precise calculation of the relativistic light bending model to study whether this model can explain the two features simultaneously. The ray-tracing technique is adopted to compute photon paths under the strong gravitational field. We select IRAS 13224–3809 as a representative object to investigate such Fe-K time features; it has the strong Fe-K spectral feature, the deep rms dip, and the significant reverberation lags. In addition, this source was observed with a very large program of *XMM-Newton*, and we are benefitted by rich photon statistics to investigate detail of the spectral variations. The iron line is strongly skewed (e.g., Boller et al. 2003), the X-ray flux shows strong variability by more than one order of magnitude with a timescale of ~ 500 s (e.g., Dewangan et al. 2002), and the rms dip has an amplitude of $\sim 50\%$ (e.g., Yamasaki et al. 2016). Kara et al. (2013a) also reported the Fe-K reverberation lags.

We try to explain all the Fe-K properties in this object. First, we explain our models in §2, and show the resultant rms spectra and lag features in §3. Then we discuss whether the model can simultaneously explain the observed rms spectra and lag features of IRAS 13224–3809 in §4, and finally state our conclusions in §5.

2 Model and assumption

We briefly explain the model used in this paper (see details in Appendix 1). We show in figure 1 the schematic picture for the model. A distant observer observes the iron line reverberation due to a static X-ray emitter close to the prograde geometrically-thin accretion disc around a rotating BH. The lamp post is assumed to emit isotropic X-ray pulses in its inertial frame. The gas element of the accretion disc is postulated to be in Keplerian motion, and the velocity components in the radial and polar directions are neglected. Radii of the inner and outer edges of the disc are fixed to be r_{ms} and $100 R_g$, respectively, where r_{ms} is the radius of the marginally stable orbit. The r_{ms} value is calculated as

$$\frac{r_{\text{ms}}}{R_g} = 3 + Z_2 - \sqrt{(3 - Z_1)(3 + Z_1 + 2Z_2)} \quad (1)$$

$$Z_1 = 1 + (1 - a^2)^{1/3} \{ (1 + a)^{1/3} + (1 - a)^{1/3} \}$$

$$Z_2 = \sqrt{3a^2 + Z_1^2},$$

where $a = J/M_{\text{BH}}^2$ is a spin parameter and J is the angular momentum of the BH. The light bending effects, Doppler effects, and gravitational redshift are taken into account. The total mass of the disc is assumed to be negligible compared to the BH mass.

We numerically calculate trajectories of the photons emitted from the static source with a point-like geometry. Some photons directly reach the observer along the path ℓ_p , which is regarded as the primary component. Other photons illuminate the accretion disc along the path ℓ_d and causes the fluorescent iron line and the reflected continuum emission, which reach the observer along the path ℓ_r . We assume the lamp post located on the rotation axis (e.g., model A in Niedźwiecki & Miyakawa 2010). For the ease of numerical calculation, intrinsic luminosity of the primary source is assumed to be invariable, and thus only changes of h_s above the disc induce observed variability. Here, we point out that the rms spectral shape is invariable even if the intrinsic luminosity is variable, unless there is significant intrinsic *spectral* variations. The observed spectra were computed for different h_s . The heights ($h = h_s/R_g$) were linearly spaced with $\Delta h = 1$ at $h \geq 3$ and $\Delta h = 0.2$ at $h < 3$, following Niedźwiecki & Miyakawa (2010). The h range was set to be $2.2 \leq h \leq 10$. Calculations are performed for four types of spin parameters ($a = 0, 0.6, 0.9, 0.998$). The photon index of the primary power-law spectrum is fixed at 2. We assume a high inclination angle ($i = 60$ deg), which is applicable for IRAS 13224–

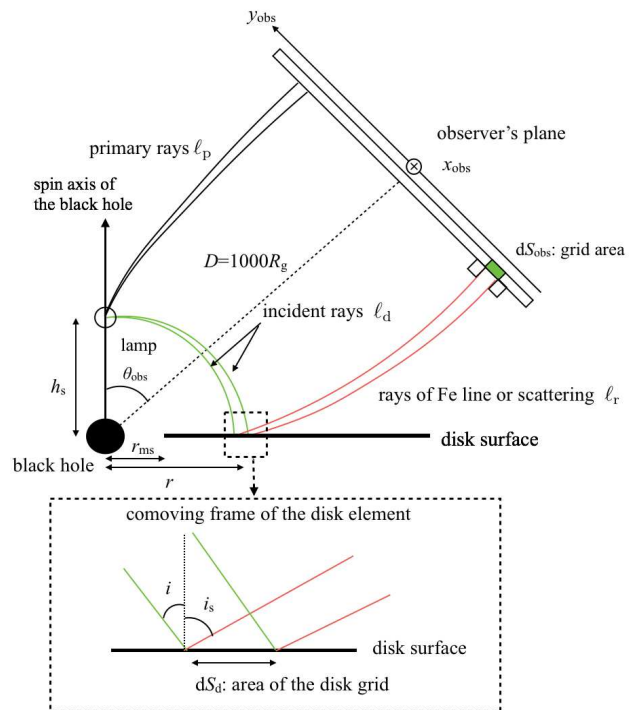


Fig. 1. Schematic picture of the relativistic light bending model. The X-ray emitter has the point-like geometry and radiates an isotropic X-ray flare in its inertial frame. The accretion disc lies in the equatorial plane and is geometrically-thin and optically-thick. The radius of the inner edge of the disc is equal to that of the marginally stable orbit, r_{ms} . Here, h_s is the height of the source, θ_{obs} is the viewing angle, and D is the distance between the BH and the centre of the observer's plane. ℓ_p , ℓ_d , and ℓ_r represent the photon path lengths of the primary, incident, and scattering orbits, respectively. Area elements of the observer's plane and the disc surface are denoted as dS_{obs} and dS_d , respectively. In the comoving frame of the disc element, i and i_s are the incident and scattering angles, respectively. The x_{obs} -axis is parallel to the equatorial plane of the BH (\otimes), and the y_{obs} -axis is perpendicular to the x_{obs} -axis.

3809 (Boller et al. 1997; Parker et al. 2017). Calculations for the low-inclination case ($i = 30$ deg) are described in Appendix 2.

3 Results

3.1 Energy spectra

Figure 2 shows h dependence of the primary and reflected spectra for different a . Find the red lines in the top left panel for explanation ($a = 0$ and $h = 9$ case): The horizontal line shows the primary spectrum, whereas the curved one shows the reflected spectrum. In the reflected spectrum, Fe-K lines, as well as the absorption edges, are skewed due to the gravitational redshift and the Doppler effect. As h decreases (see other colours in the same panel), the effect of the gravitational redshift becomes stronger, fewer photons escape from the gravitational field, and both the observed iron line fluxes and the primary component become smaller. On the other hand, Doppler effect of the disc

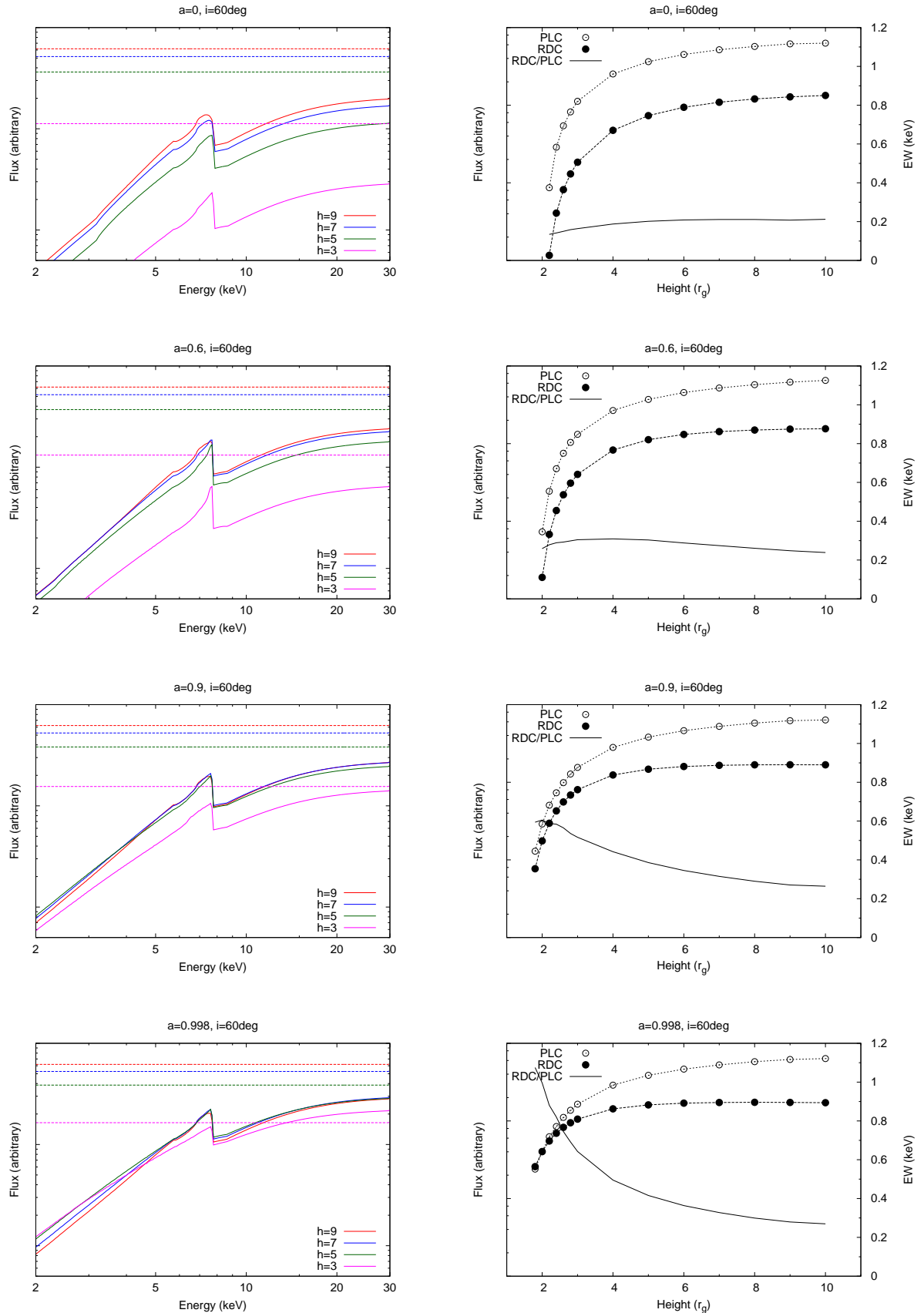


Fig. 2. (Left) Primary and reflected (iron line + Compton reflection) spectra for different a and h , shown by dashed and solid lines, respectively. The vertical axis shows the energy flux (an arbitrary unit). (Right) The PLC (flux at 6.4 keV) and RDC (integrated over the iron line) fluxes as a function of h . The iron line EW \equiv RDC/PLC is also shown in the solid line. Units of flux are arbitrary, whereas that of EW is given in keV.

has little dependence on h , such that the cut-off energies of the blue lines are unchanged. When a increases (see red lines in the other panels), the inner edge of the disc moves inward and the line is more strongly skewed by the gravitational redshift. Therefore, the low-energy tail reaches the softer band and the Fe-K emission line becomes broader.

The right panel of figure 2 shows variations of the PLC flux, the RDC flux, and the equivalent widths (EW) of the iron line (=RDC flux/PLC flux), where the PLC flux shows the 6.4 keV flux and the RDC flux shows the integrated flux over the iron line (Miniutti & Fabian 2004). When $a \lesssim 0.6$, variations of the RDC and PLC fluxes are similar, so the EW is rather flat against significant change of h . In the larger spin cases ($a > 0.9$), the RDC flux is almost flat due to the light-bending effect in the h range of $\sim 5 - 10$ while the PLC flux is more significantly variable; this is considered to be the cause of the Fe-K dip in the rms spectrum.

3.2 Spectral variability

We compute 12 simulated spectra for different h ($= 2.2 - 10$) and calculated fractional variability amplitudes (F_{var} ; Edelson et al. 2002) using the following equation:

$$F_{\text{var}}(E) = \frac{1}{\langle X \rangle} \sqrt{S^2 - \langle \sigma_{\text{err}}^2 \rangle}, \quad (2)$$

where X_i is the photon count in the energy bin of interest for the i -th among the 12 simulated spectra, $\langle X \rangle$ is the mean counts, S^2 is the variance of $\{X_i\}$, and $\langle \sigma_{\text{err}}^2 \rangle$ is the mean error squared of $\{X_i\}$, which is assumed to be null in our calculations. We assume that h varies continuously between 2.2 and 10. We also calculate the rms spectra assuming different variation pattern of h (such that h variation follows the sinusoidal function), only to find that the resultant rms features hardly change.

Figure 3 shows the resultant rms spectra. In the zero spin case, variations of PLC and RDC are similar and EW of the iron line is constant against different h (figure 2), so the rms spectrum is rather featureless. In the spinning case, RDC varies less than PLC (figure 2), and both Compton reflection and iron line reduce variation amplitudes. In particular, the rms dip gets deeper and broader for the higher spin ($a \geq 0.9$). The relative dip depths at the 7–8 keV band are up to 20% in the maximum spin case.

3.3 Time lags

Next, we compute time lags (also see Mizumoto et al. 2018). Here, the time lag is defined as

$$\tau(f) = \arg[\mathcal{S}(f)\mathcal{H}^*(f)]/(2\pi f), \quad (3)$$

where $*$ means complex conjugate and $\mathcal{S}(f)$ and $\mathcal{H}(f)$ are Fourier transforms of soft- and hard-band light curves, $s(t)$ and $h(t)$ (Vaughan & Nowak 1997; Nowak et al. 1999). We use the

3–4 keV (less contaminated by the reflected component) for the soft band and 5–8 keV (dominated by the reflected one) for the hard band. A positive lag means the hard band lagging the soft, and vice versa. An observed light curve is expressed as the sum of the primary emission and the reprocessed emission. Now we assume that the primary emission is expressed as $P(E)g(t)$, where $P(E)$ is the spectrum of the primary component and $g(t)$ is the intrinsic flux variability. We define $R(E, k)$ as photon counts of the reflected component in each energy-bin (E) and time-bin (k). In this setting, the light curves are written as

$$s(t) = P_s g(t) + \sum_k R_s(k) g(t - kt_{\text{bin}}) \quad (4)$$

$$h(t) = P_h g(t) + \sum_k R_h(k) g(t - kt_{\text{bin}}), \quad (5)$$

where t_{bin} is a time bin-size of the light curve and $P_{s,h}$ and $R_{s,h}(E)$ are the primary components and the reflected components, respectively, and the suffixes indicate the energy bands. Their Fourier transforms are expressed as

$$\mathcal{S}(f) = P_s \mathcal{G}(f) + \sum_k R_s(k) \exp[-2\pi i(kt_{\text{bin}})f] \mathcal{G}(f) \quad (6)$$

$$\mathcal{H}(f) = P_h \mathcal{G}(f) + \sum_k R_h(k) \exp[-2\pi i(kt_{\text{bin}})f] \mathcal{G}(f), \quad (7)$$

where $\mathcal{G}(f)$ are Fourier transform of $g(t)$. Unless $\mathcal{G}(f) = 0$, equation (3) is calculated as

$$\tau(f) = \frac{1}{2\pi f} \arg \left[\left(P_s + \sum_k R_s(k) \exp[-2\pi i(kt_{\text{bin}})f] \right) \left(P_h + \sum_k R_h(k) \exp[2\pi i(kt_{\text{bin}})f] \right) \right]. \quad (8)$$

Note that *this equation does not depend on the functional form of the intrinsic variation*. $P(E)$ and $R(E, k)$ are directly calculated from our simulations. $P(E)$ corresponds to the primary component in figure 2. Figure 4 shows $R(E, k)$, i.e., counts of the reflected photons in each time- and energy-bin. This corresponds to the two-dimensional (2D) transfer function applied to the input photon spectrum. Interpretation of the 2D transfer functions are described in previous papers (e.g., Reynolds et al. 1999; Wilkins & Fabian 2013; Cackett et al. 2014). The delay time of a scattered photon is determined by the photon path difference from the primary photons, as well as Shapiro delays. The main difference among different a is that the energy-averaged responses in the high-spin cases have stronger peaks than in the low-spin cases. This difference is because the disc with high a has a larger surface area than that with low a and extends closer to the BH, whereas the response from the outer part of the disc is still the same (also see Cackett et al. 2014).

First, we calculate the lags for each fixed h value. We assume that the BH mass is $10^{6.8} M_{\odot}$ (González-Martín & Vaughan 2012), i.e., $R_g/c = 30$ s. The black dotted lines in figure 5 shows the lag-energy plots of each h value. The lag

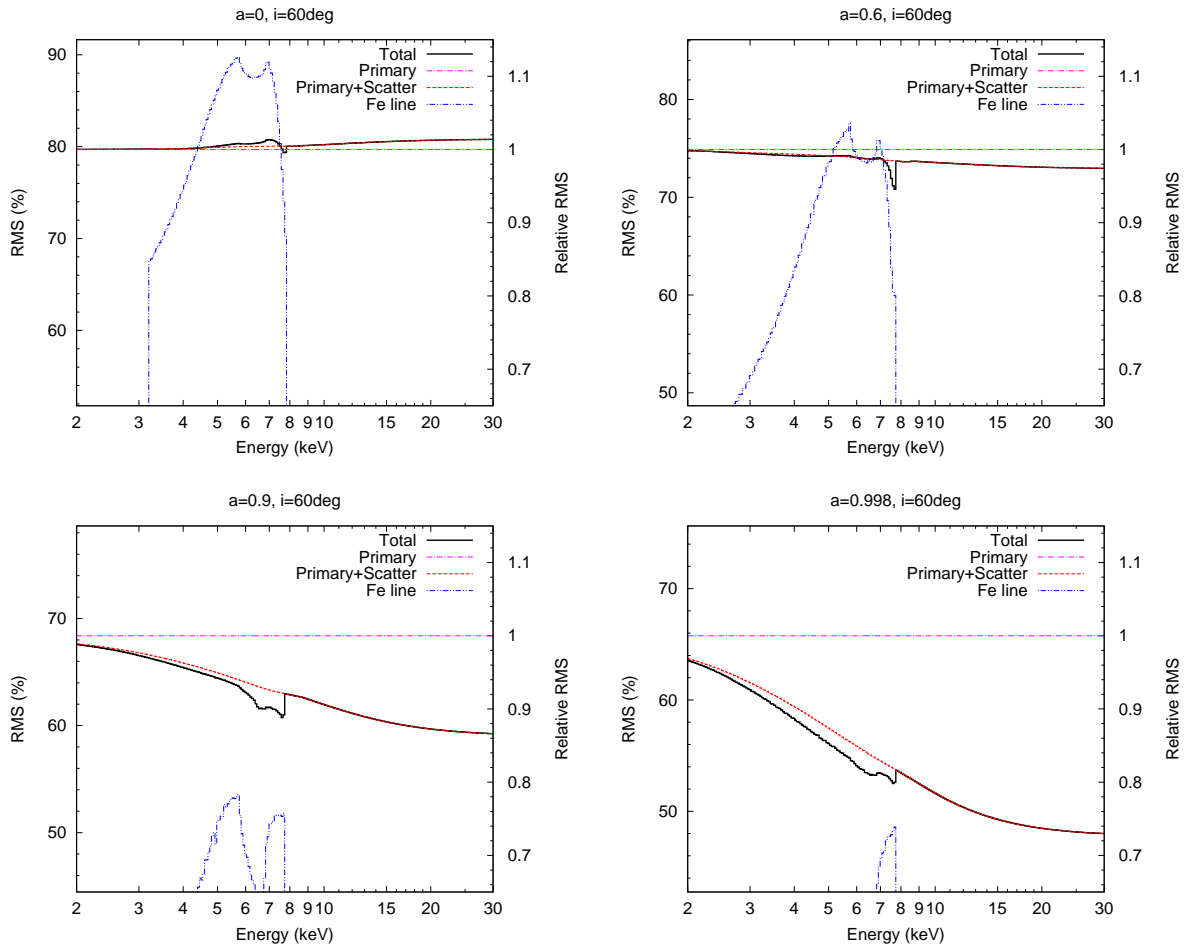


Fig. 3. The rms spectra for different spectral components. The curves are for the primary component (magenta dot-dashed), the primary+Compton reflection (red dashed), and the iron line (blue dot-dot-dashed). The black solid curve indicates the total emission (primary+Compton reflection+iron line). The right axis show the relative amplitude where that of primary component is normalised as unity.

amplitude at the lowest frequency decreases with lower h corresponding to the light-travel time, but above the pivot point at $\sim [1 - 5] \times 10^{-4}$ Hz, the lag amplitude increases. Next, with the probability distribution of h being flat within the variation range of $h = 2.2 - 10$, we calculate the average lag-frequency plot (red-solid line in figure 5). The lag amplitude in the high frequency range ($\gtrsim 5 \times 10^{-4}$ Hz) is larger for larger a because reflection on the innermost part of the disc is stronger.

Figure 6 shows the lag-energy spectra for different a in the high frequency range (8×10^{-4} Hz). We compute a lag between each energy band of interest and a broad reference band of 2–30 keV. All energy bins include both the primary and disc-reflection components, regardless of which dominates in the bins. This means that the dilution effects are fully taken into account. The reverberation Fe-K lags are seen in all the cases, but the broad features in the 4–8 keV band are only seen when $a > 0.9$. The lag amplitude is in the range of 1–2 R_g/c .

4 Discussion

4.1 Comparison with observations of IRAS 13224–3809

Our calculations show that the Fe-K rms dip ($\lesssim 20\%$) and the broad Fe-K lag with the amplitude of ~ 50 s are seen when $a > 0.9$. Here, we carefully investigate whether these results can quantitatively explain observations of IRAS 13224–3809.

4.1.1 rms spectra

Figure 7 shows the observed rms spectrum of IRAS 13224–3809, in which results in the previous section are overplotted. We use all the archival data of this object with *XMM-Newton* between 2002 and 2016, whose total exposure time is 1.46 Ms. These data were reduced with the Science Analysis System (SAS) v15.0.0, the latest calibration files, and the standard threads of SAS. We manually discarded high-background periods to get consecutive data as long as possible in each sequence. A time-bin width of the rms spectra is 1500 s, which

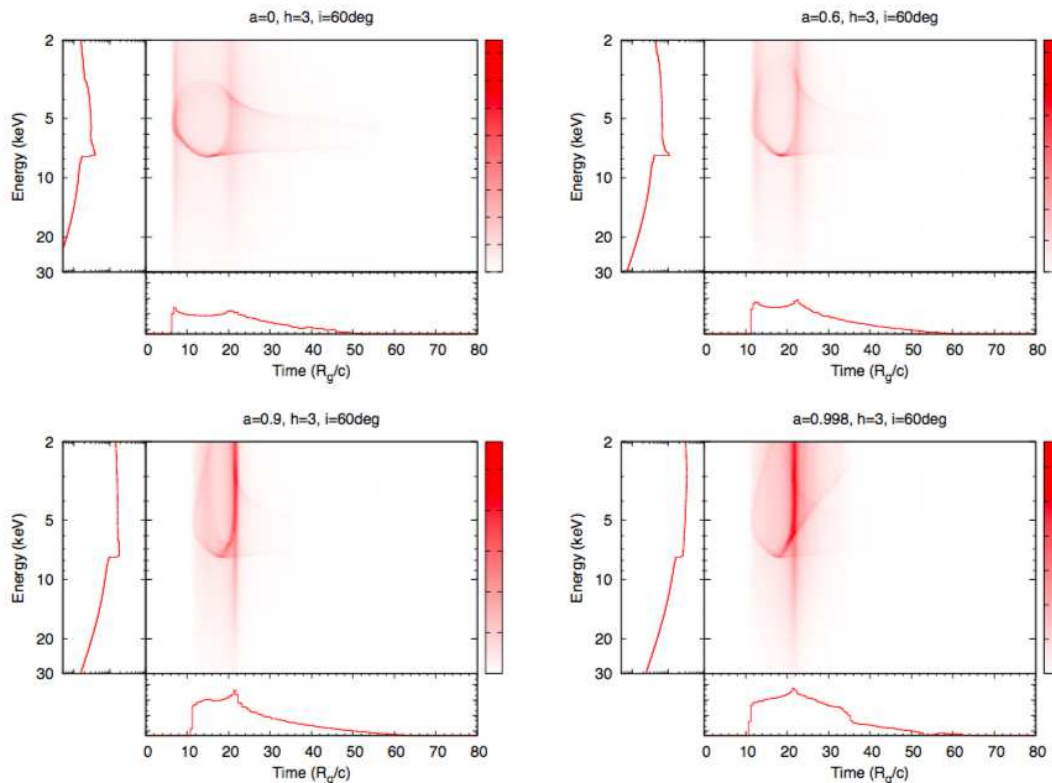


Fig. 4. Main panels: Counts of the photons reflected on the disc for different i and a when $h = 3$. The X-ray source emits at once with a delta-function of time. The color bar shows the photon counts in the arbitrary unit. Left-hand panels: Projection to the y -axis, which gives the total energy spectrum of all the reflected photons. Bottom panels: Projection to the x -axis, which gives the energy-averaged response

corresponds to the frequency investigated in the lag features ($[5.8 - 10.5] \times 10^{-4}$ Hz). The variability amplitude at 7 keV is 55%, whereas that at 2 keV is 98%. In our calculations, when h varies within $2.2 - 10$ (red dashed in figure 7), the rms dip is produced but the depth is too shallow to explain the observation. We calculated the rms spectra with different h ranges (green dotted and magenta dot-dashed in figure 7), but none can explain the observed feature. Therefore we conclude that the observed rms dip cannot be explained by the relativistic disc reflection model as far as the iron abundance is solar.

Next, we intentionally change the iron line flux to explain the deep rms dip. We manually increase the iron flux by ten times, equivalently 10 solar overabundance of iron, and calculate the rms spectra. As a result, the observed deep dip can be almost reproduced (blue solid). Therefore, we see that the extreme iron overabundance ($\gtrsim 10$ solar) is required to explain the rms dip with the relativistic light bending model.

4.1.2 Lag features

We calculate the lag-energy spectrum of IRAS 13224–3809 in the frequency range of $[5.8 - 10.5] \times 10^{-4}$ Hz (figure 8), following Kara et al. (2013a). We use the same data in the rms spectrum. The Fe-K lag amplitude is about 80 s, which corresponds to $\sim 2 - 3 R_g/c$. Indeed, the lag-energy plot obtained by

our simulation is consistent with the observed one (red dashed). The lag amplitude becomes longer as the iron line flux (with time delay) is stronger. The magenta line in figure 8 shows the case when the iron flux is doubled, which is still acceptable. However, when the iron flux is ten times stronger (blue line), the lag amplitude gets more than 150 s, which is clearly rejected. Thus, the iron abundance constrained by the lag feature ($\sim 1 - 2$ solar) contradicts the one derived from the rms dip ($\gtrsim 10$ solar).

Kara et al. (2013a) reported flux-dependence of the Fe-K lags in this object. They examined lags from low- and high-flux intervals, where average count rates are different by one order of magnitudes. The Fe-K lags disappear in the high-flux period for $[1.4 - 2.8] \times 10^{-4}$ Hz, whereas they are seen in the low-flux period for $[5.8 - 10.5] \times 10^{-4}$ Hz (figure 6 in Kara et al. 2013a). In the framework of the relativistic light bending model, this change may be explained by significant change of the lamp post height. As the lamp post height varies, the RDC flux is hardly variable and the PLC flux varies by an order of magnitudes, therefore the lag in the high-flux period is diluted by the strong PLC component. However, our calculation indicates that the reverberation lag is still clearly seen even when $h = 20$ (figure 9). Assuming that the frequency where the lag amplitude gets to zero monotonically decreases with larger h , the height where

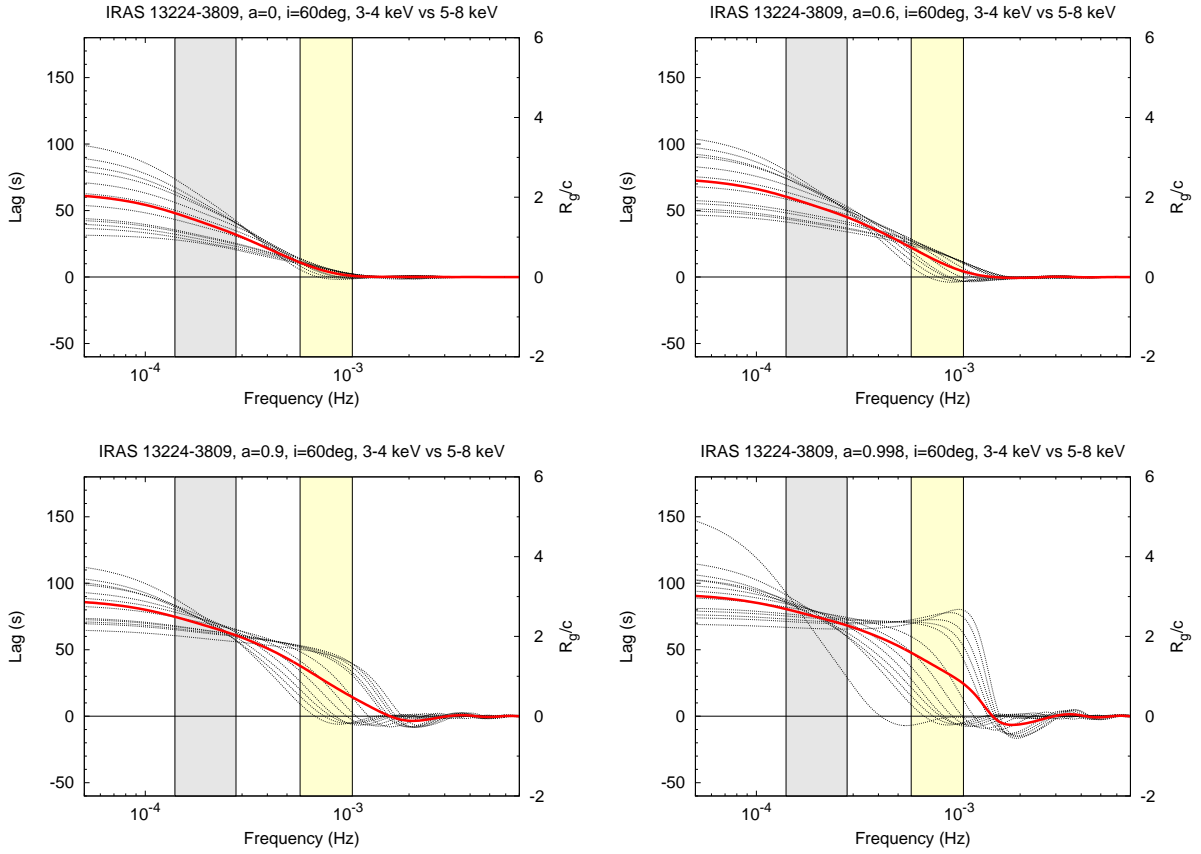


Fig. 5. Lag-frequency plots, comparing 3–4 keV with 5–8 keV, with h values of 2.2, 2.4, 2.6, 2.8, 3.0, 4.0, 5.0, ..., 10.0 from bottom to top at the lowest frequency. A positive lag means that the hard band lags behind the soft. The BH mass is $10^{6.8} M_{\odot}$, i.e., $R_g/c = 30$ s, assuming IRAS 13224–3809. The yellow area shows $[5.8 - 10.5] \times 10^{-4}$ Hz where the Fe-K lag is prominently seen in IRAS 13224–3809, and the grey shows $[1.4 - 2.8] \times 10^{-4}$ Hz where the lag disappears in the high-flux periods of the same source. The red solid line shows the average plot in $h = 2.2 - 10$. The plot of $h = 20$ is additionally shown only in the $\alpha = 0.998$ case.

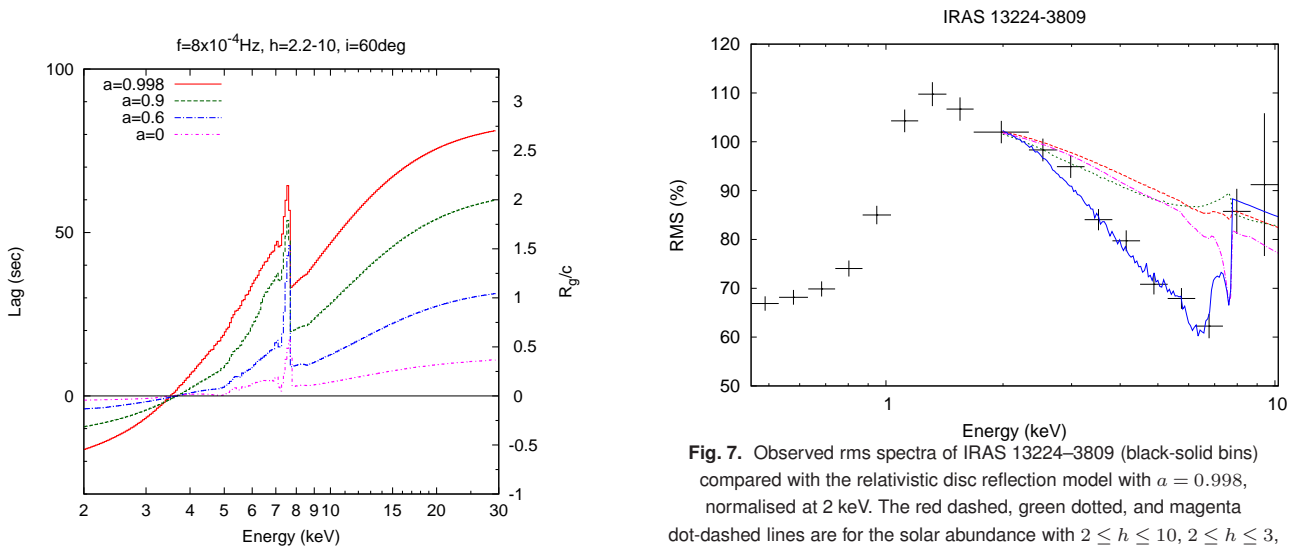


Fig. 6. Lag-energy plots for different α at the frequency of 8×10^{-4} Hz

Fig. 7. Observed rms spectra of IRAS 13224–3809 (black-solid bins) compared with the relativistic disc reflection model with $\alpha = 0.998$, normalised at 2 keV. The red dashed, green dotted, and magenta dot-dashed lines are for the solar abundance with $2 \leq h \leq 10$, $2 \leq h \leq 3$, and $5 \leq h \leq 10$, respectively. The blue solid line is for 10 times overabundance of iron with $2 \leq h \leq 10$.

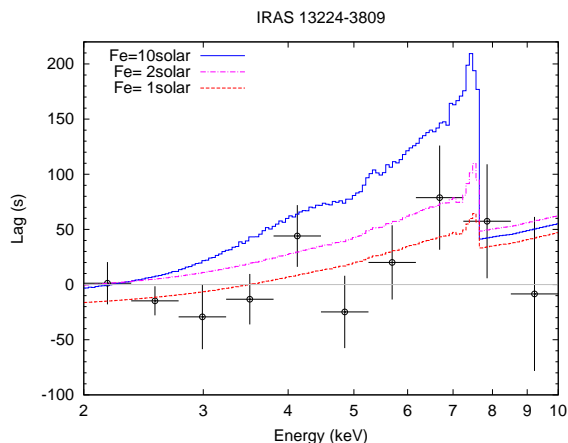


Fig. 8. Observed lag-energy spectrum of IRAS 13224–3809 (black bins) in the frequency range of $[5.8 - 10.5] \times 10^{-4}$ Hz, compared with the relativistic disc reflection model with $a = 0.998$. The red dashed, magenta dot-dashed, and blue solid lines show when the iron abundance is equal to, twice, and 10 times of the solar abundance, respectively. The zero point in both the data and model lines corresponds to the reference band of 2–10 keV.

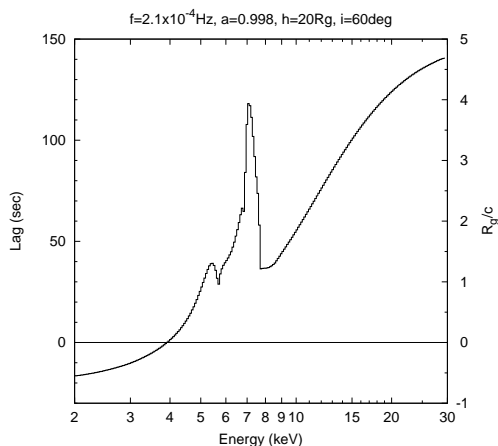


Fig. 9. Lag-energy plots for $h = 20 R_g$ and $a = 0.998$ at the frequency of 2.1×10^{-4} Hz.

the lag disappears should be $\sim 40 R_g$. However, this clearly contradicts the observed line profile; the line is hardly skewed and broadened with such a large source height (e.g., Fabian et al. 2002).

4.2 On the black-hole spin constraint

Some authors claimed that spin of IRAS 13224–3809 is tightly constrained to be almost maximum based on model fitting of the X-ray spectra, e.g., $0.990^{+0.001}_{-0.003}$ and 0.988 ± 0.001 (Fabian et al. 2013; Chiang et al. 2015). They proposed extremely-high emissivity indices $q (\gtrsim 9)$, where the disc emissivity per area at a radius r is proportional to r^{-q} . When the emissivity index is so high, the reflection component from the inner region of the disc is fully dominant, and thus the Fe-K line profiles are extremely sensitive to small change of a (i.e. change of r_{ms}). We calculate

the emissivity profiles and indices from our simulations (figure 10). In this figure, the emissivity index is up to ~ 6 at the innermost edge of the disc with the source height of $2 R_g$ even in the maximum spin case, and such a high emissivity index of $q \gtrsim 9$ is possible only when the lamp locates within $2 R_g$ from the central BH. Thus, the spin parameters cannot be constrained unless the source height is extremely small (see also Bonson & Gallo 2016). However, our model requires significant height variations (typically $h = 2 - 10$) to produce the observed Fe-K rms dip (figure 7). Also, we might tell whether $a < 0.9$ or $a > 0.9$ from the time variability, but it is difficult to distinguish $a = 0.9$ from $a = 0.998$ (figures 3, 6).

The situation becomes more complex since other mechanisms also affect the Fe-K spectral feature. Noda et al. (2011) pointed out that the iron line profiles are easily changed when the continuum level is different. In addition, absorption features can mimic the broad emission line; when the cold clumpy absorbers partially cover the X-ray source, a broad Fe-K absorption edge is produced (e.g., Tanaka et al. 2004; Miyakawa et al. 2012; Mizumoto et al. 2014; Iso et al. 2016; Yamasaki et al. 2016), and when the strong ultrafast outflow exists in the line of sight (e.g., Tombesi et al. 2010), the broad and blueshifted absorption line features due to H- or He-like iron ion are seen in the energy spectra (Hagino et al. 2015, 2016). These absorption features affect the iron line profile, and thus we suggest that the BH spin values estimated from Fe-line spectral fitting or time variations are not reliable.

5 Conclusion

Seyfert galaxies are known to exhibit characteristic spectral variability; root-mean-square (rms) dips in the Fe-K energy band and the Fe-K reverberation lags. The relativistic light bending model, where a lamp post is moving vertically along the rotation axis, has been proposed to explain these features. We critically examined whether the relativistic light bending model can explain the two features simultaneously. A ray-tracing technique is adopted including the full treatment of general relativity to calculate photon paths and delay times of the reflection. We try to explain Fe-K features of IRAS 13224–3809, which is a representative source to exhibit the characteristic Fe-K features. The observed rms dip may be reproduced when an extreme iron overabundance ($\gtrsim 10$ solar) is assumed. On the contrary, the observed lag-energy spectrum requires solar abundance of iron; it clearly rejects the extreme iron overabundance. In addition, the observed diminution of the lag feature in the high-flux state needs a very large source height of $\sim 40 R_g$, which contradicts the observed broad line profile. Consequently, we conclude that the relativistic light bending model cannot explain both the rms dips and reverberation lags in the Fe-K band simultaneously. BH spin parameters constrained

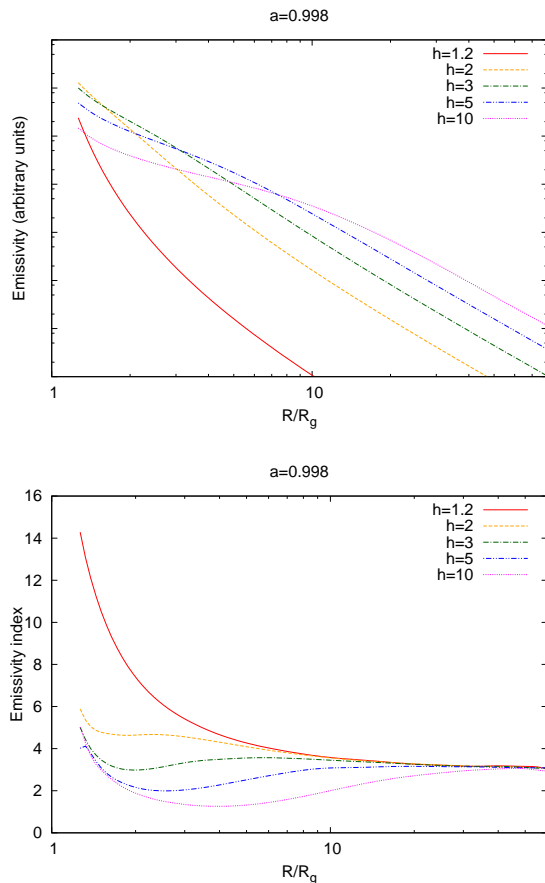


Fig. 10. (Upper) Disc emissivity profiles, $\epsilon(r)$, calculated by our ray-tracing method for different lamp-post heights. (Lower) Emissivity indices, q , which is defined by $\epsilon(r) \propto r^{-q}$.

by this model are thus not reliable.

Acknowledgments

Authors are financially supported by the JSPS/MEXT KAKENHI Grant Numbers JP15J07567 (MM), JP17J08829 (KM), JP16K05309 (KE), and JP24105007, JP15H03642 (MT). NK is supported by the Hakubi project in Kyoto University.

References

- Boller, T., Brandt, W. N., Fabian, A. C., & Fink, H. H. 1997, *MNRAS*, 289, 393
- Boller, T., Tanaka, Y., Fabian, A., et al. 2003, *MNRAS*, 343, L89
- Bonson, K. & Gallo, L. C. 2016, *MNRAS*, 458, 1927
- Cackett, E. M., Zoghbi, A., Reynolds, C., et al. 2014, *MNRAS*, 438, 2980
- Chiang, C.-Y., Walton, D. J., Fabian, A. C., Wilkins, D. R., & Gallo, L. C. 2015, *MNRAS*, 446, 759
- Dewangan, G. C., Boller, T., Singh, K. P., & Leighly, K. M. 2002, *A&A*, 390, 65
- Edelson, R., Turner, T. J., Pounds, K., et al. 2002, *ApJ*, 568, 610
- Emmanoulopoulos, D., Papadakis, I. E., Dovčiak, M., & McHardy, I. M. 2014, *MNRAS*, 439, 3931

- Fabian, A. C., Ballantyne, D. R., Merloni, A., et al. 2002, *MNRAS*, 331, L35
- Fabian, A. C., Kara, E., Walton, D. J., et al. 2013, *MNRAS*, 429, 2917
- Fabian, A. C., Rees, M. J., Stella, L., & White, N. E. 1989, *MNRAS*, 238, 729
- Fabian, A. C. & Vaughan, S. 2003, *MNRAS*, 340, L28
- Fabian, A. C., Zoghbi, A., Ross, R. R., et al. 2009, *Nature*, 459, 540
- González-Martín, O. & Vaughan, S. 2012, *A&A*, 544, A80
- Hagino, K., Odaka, H., Done, C., et al. 2015, *MNRAS*, 446, 663
- Hagino, K., Odaka, H., Done, C., et al. 2016, *MNRAS*, 461, 3954
- Inoue, H. & Matsumoto, C. 2003, *PASJ*, 55, 625
- Iso, N., Ebisawa, K., Sameshima, H., et al. 2016, *PASJ*, 68, S27
- Kara, E., Alston, W. N., Fabian, A. C., et al. 2016, *MNRAS*, 462, 511
- Kara, E., Fabian, A. C., Cackett, E. M., Miniutti, G., & Uttley, P. 2013a, *MNRAS*, 430, 1408
- Kara, E., Fabian, A. C., Cackett, E. M., et al. 2013b, *MNRAS*, 428, 2795
- Karas, V., Vokrouhlický, D., & Polnarev, A. G. 1992, *MNRAS*, 259, 569
- Laor, A. 1991, *ApJ*, 376, 90
- Matsumoto, C., Inoue, H., Fabian, A. C., & Iwasawa, K. 2003, *PASJ*, 55, 615
- Miniutti, G. & Fabian, A. C. 2004, *MNRAS*, 349, 1435
- Miniutti, G., Fabian, A. C., Goyder, R., & Lasenby, A. N. 2003, *MNRAS*, 344, L22
- Miyakawa, T., Ebisawa, K., & Inoue, H. 2012, *PASJ*, 64, 140
- Mizumoto, M., Done, C., Hagino, K., et al. 2018, *MNRAS*, submitted
- Mizumoto, M., Ebisawa, K., & Sameshima, H. 2014, *PASJ*, 66, 122
- Moriyama, K. & Mineshige, S. 2015, *PASJ*, 67, 106
- Morrison, R. & McCammon, D. 1983, *ApJ*, 270, 119
- Niedźwiecki, A. & Miyakawa, T. 2010, *A&A*, 509, A22
- Noda, H., Makishima, K., Uehara, Y., Yamada, S., & Nakazawa, K. 2011, *PASJ*, 63, 449
- Nowak, M. A., Vaughan, B. A., Wilms, J., Dove, J. B., & Begelman, M. C. 1999, *ApJ*, 510, 874
- Parker, M. L., Pinto, C., Fabian, A. C., et al. 2017, *Nature*, 543, 83
- Pious, J. K., Balakrishna, K. M., Lingappa, N., & Siddappa, K. 1992, *J. Phys. B: At. Mol. Opt. Phys.*, 25, 1155
- Reynolds, C. S., Young, A. J., Begelman, M. C., & Fabian, A. C. 1999, *ApJ*, 514, 164
- Tanaka, Y., Boller, T., Gallo, L., Keil, R., & Ueda, Y. 2004, *PASJ*, 56, L9
- Tanaka, Y., Nandra, K., Fabian, A. C., et al. 1995, *Nature*, 375, 659
- Terashima, Y., Gallo, L. C., Inoue, H., et al. 2009, *PASJ*, 61, S299
- Tombesi, F., Cappi, M., Reeves, J. N., et al. 2010, *A&A*, 521, A57
- Žycki, P. T., Ebisawa, K., Niedźwiecki, A., & Miyakawa, T. 2010, *PASJ*, 62, 1185
- Vaughan, B. A. & Nowak, M. A. 1997, *ApJL*, 474, L43
- Wilkins, D. R. & Fabian, A. C. 2013, *MNRAS*, 430, 247
- Yamasaki, H., Mizumoto, M., Ebisawa, K., & Sameshima, H. 2016, *PASJ*, 68, 80
- Yoshida, H. 1993, *Celestial Mechanics and Dynamical Astronomy*, 56, 27
- Zoghbi, A., Fabian, A. C., Reynolds, C. S., & Cackett, E. M. 2012, *MNRAS*, 422, 129

Appendix 1 Numerical calculation of the relativistic light bending model

We explain details of the relativistic light bending model and the numerical calculation methods used in this paper. In this section, we use “geometrised units” in which G and c are set to be unity.

A.1.1 Relativistic light bending model

First, we consider the photons to directly reach the observer. The height, radial position and 4-velocity of the source are denoted by h_s , ρ_s and $u_s^\mu = (u_s^0, 0, 0, u_s^3)$ (see figure 1). In its inertial frame, the radiation energy per unit time, and energy, $dW_\ell(e_\ell, t)/dt$, is defined as

$$\frac{dW_\ell(e_\ell, t)}{dt} de_\ell = N e_\ell^{-\Gamma+1} \delta(t) de_\ell, \quad (\text{A1})$$

where N is the photon number, e_ℓ is the photon energy, t is the Boyer-Lindquist time coordinate, and $\Gamma (= 2)$ is the spectral index. The primary continuum emission to reach directly to the observer from the emitter is expressed as

$$\begin{aligned} \frac{dW_p(e_{\text{obs}}, t)}{dt} de_{\text{obs}} &= g_0^2 \frac{dW_\ell(e_\ell, t - \tau_p)}{dt} de_\ell \\ &= g_0^\Gamma N e_{\text{obs}}^{-\Gamma+1} \delta(t - \tau_p) de_{\text{obs}}, \end{aligned} \quad (\text{A2})$$

where e_{obs} is the observed photon energy, and $\tau_p (= \ell_p)$ is the time taken for a photon from the source to reach the observer's plane. Further, g_0 is the energy-shift factor between the observer and source, and is written as

$$g_0 = \frac{e_{\text{obs}}}{e_\ell} = \frac{1}{u_\ell^0 (1 - \Omega_\ell \Lambda)}, \quad (\text{A3})$$

where $\Omega_\ell = u_\ell^3 / u_\ell^0$ is the angular velocity of the source, and Λ is the angular momentum of the photon with respect to the azimuth direction (ϕ) per energy. Therefore, the total photon flux to reach the observer, $F_p(e_{\text{obs}}, t) de_{\text{obs}}$, is written as

$$F_p(e_{\text{obs}}, t) de_{\text{obs}} = g_0^\Gamma N'_p e_{\text{obs}}^{-\Gamma} \delta(t - \tau_p) de_{\text{obs}}, \quad (\text{A4})$$

where N'_p is the photon number to reach the observer's plane per unit area.

Next, we consider the incident photon in the comoving frame of the accretion disc. The incident energy flux entering the gas element of the disc located at (r, ϕ) , is expressed as

$$\begin{aligned} \frac{dW_d(e_d, t)}{dt dS_d} de_d &= g_1^2 \frac{dW_\ell(e_\ell, t - \tau_d)}{dt dS_d} de_\ell \\ &= g_1^\Gamma N'_d e_d^{-\Gamma+1} \delta(t - \tau_d) de_d, \end{aligned} \quad (\text{A5})$$

where N'_d is the incident photon number per unit area, dS_d is the disc area element, e_d is the energy of the incident photon in the comoving frame, and τ_d is the photon path length between the source and gas element (see figure 1). Further, the energy shift factor between the source and disc, g_1 , is written by

$$g_1 = \frac{u_d^0 (1 - \Omega_d \Lambda)}{u_\ell^0 (1 - \Omega_\ell \Lambda)}, \quad (\text{A6})$$

where u_d^μ and Ω_d is the 4-velocity and angular velocity of the disc element.

Photons in the fluorescent $K\alpha$ line and the reflected continuum from the disc element are regarded as the reflection component. Probabilities that the fluorescent $K\alpha$ line (6.4 keV at the rest frame) and the reflected continuum are emitted from the disc element, $P_{K\alpha}$ and P_{scat} , are expressed as

$$P_{K\alpha}(e_d) = W_K \frac{\sigma_a(e_d)}{\sigma_a(e_d) + \sigma_s(e_d)}, \quad (\text{A7})$$

$$P_{\text{scat}}(e_d) = \frac{\sigma_s(e_d)}{\sigma_a(e_d) + \sigma_s(e_d)}, \quad (\text{A8})$$

where e_d is the energy of the incident photon in the comoving frame, $W_K [= 0.35 (0) \text{ for } e \geq E_e = 7.112 \text{ keV } (e < E_e)]$ is the iron $K\alpha$ fluorescence yield (Pious et al. 1992), $\sigma_a(e)$ is the iron photoelectric absorption cross-section (table 2 in Morrison & McCammon 1983), and $\sigma_s(e)$ is the electron scattering cross-section given by the Klein-Nishina formula, such as

$$\sigma_a(e) = \sigma_T \frac{3}{4} \left[\frac{1+e}{e^3} \left\{ \frac{2e(1+e)}{1+2e} - \ln(1+2e) \right\} + \frac{\ln(1+2e)}{2e} - \frac{1+3e}{(1+2e)^2} \right],$$

where σ_T is the Thomson cross-section.

In the comoving frame of the gas element at (r, ϕ) , reflected photon flux, $F_d(e_d, t)$ is expressed as

$$F_d(e_d, t) = F_{K\alpha}(e_d, t) + F_{\text{scat}}(e_d, t), \quad (\text{A10})$$

where $F_{K\alpha}$ and F_{scat} are the photon flux of the fluorescent $K\alpha$ line and reflected continuum radiation, and are defined as

$$\begin{aligned} F_{K\alpha}(e_d, t) &= g_1^\Gamma N'_d \delta(e_d - 6.40 \text{ keV}) \delta(t - \tau_d) \int_{E_e}^\infty P_{K\alpha}(e) e^{-\Gamma} de \\ F_{\text{scat}}(e_d, t) &= g_1^\Gamma N'_d \delta(t - \tau_d) e_d^{-\Gamma} P_{\text{scat}}(e_d). \end{aligned} \quad (\text{A11})$$

Therefore the radiative energy per unit time, energy, and solid angle is written as

$$\frac{dW_{\text{rev}}(e_d, t)}{dt d\Omega dS_d} = \frac{e_d}{4\pi} F_d(e_d, t). \quad (\text{A12})$$

The emissivity of the fluorescent $K\alpha$ line, j , is proportional to $F_{K\alpha}$:

$$j(r, \phi) = J g_1(r, \phi)^\Gamma N'_d(r, \phi) \int_{E_e}^\infty P_{K\alpha}(e) e^{-\Gamma} de \quad (J = \text{const.}). \quad (\text{A13})$$

Finally, we consider the total radiation energy of the photons to reach the observer. The observed radiation emitted from a disc element located at (r, ϕ) is expressed as

$$\left[\frac{dW_{\text{obs}}(e_{\text{obs}}, t)}{dt d\Omega dS_{\text{obs}}} \right]_j = \left[\frac{g_2^2 e_{\text{obs}}}{4\pi} F_d(e_{\text{obs}}/g_2, t - \tau_r) \right]_j \quad (\text{A14})$$

$$g_2 = \frac{e_{\text{obs}}}{e_d} = \frac{1}{u^0 (1 - \Omega_d \Lambda_r)} \quad (\text{A15})$$

$$\Lambda_r = -x_{\text{obs}} \sin \theta_{\text{obs}}, \quad (\text{A16})$$

where $(dS_{\text{obs}})_j$ is the disc element, e_{obs} is the observed photon energy, τ_r is the time taken for a photon from the gas element to reach the observer's plane. The ray reaches the Cartesian coordinate on the observer's plane, $(x_{\text{obs}}, y_{\text{obs}})$, with the angular momentum of the photon with respect to the ϕ direction per energy, Λ_r (figure 1). The suffix "j" is the number of each cell of the observer's plane.

Thus the total energy flux to reach the observer's plane is expressed as

$$F_{\text{tot}} = \sum_j \left(\frac{dW_{\text{obs}}(e_{\text{obs}}, t - \tau_r)}{dt dS_{\text{obs}}} de_{\text{obs}} \right)_j$$

$$= \sum_j \left[\frac{dS_{\text{obs}}}{4\pi D^2} g_2^2 F_d(e_{\text{obs}}/g_2, t - \tau_r) \right]_j. \quad (\text{A17})$$

A.1.2 Methods of numerical calculation

We numerically calculate trajectories of the rays emitted from the static source by solving the null geodesic equation; we apply the symplectic method (Yoshida 1993; Moriyama & Mineshige 2015), where the impact parameter of each ray is given by Karas et al. (1992). In this calculation, we obtain τ_p , N'_p and g_0 , and then calculate F_p by using equation (A4). Next, we calculate trajectories to reach the disc surface from the source, and obtain τ_d , N'_d , i , and g_1 . Then we calculate $F_{K\alpha}$ and F_{scat} by using equation (A11).

We calculate ray trajectories which leave each area element of the observer's plane in the perpendicular direction to reach the disc by applying the symplectic method to obtain $\tau_r(x_{\text{obs}}, y_{\text{obs}})$, and g_2 . F_{tot} is calculated by substituting $F_{K\alpha}$, F_{scat} , $\tau_r(x_{\text{obs}}, y_{\text{obs}})$, and g_2 in equation (A17).

Appendix 2 Simulation in the low inclination case

Resultant rms spectra and lag features for $i = 60$ deg are shown in the main text. In this section, we explain those for the low inclination case, $i = 30$ deg.

Figure 11 shows h dependence of the Fe-K line profiles and fluxes for different a . Doppler effect becomes weaker and thus a narrower Fe line is produced than the $i = 60$ deg cases; the blue cut-off energy and the red horn energy are ~ 6.8 keV and ~ 5.8 keV, respectively, whereas they are ~ 8 keV and ~ 5.2 keV for $i = 60$ deg. In particular, h dependence of the line flux is very different; the peak flux of the iron line varies by one order of magnitude between $h = 3$ and 8 for $i = 30$ deg, whereas it is only a factor of 2 for $i = 60$ deg. The large RDC variability makes the EW plots rather flat. The rms dip is not produced in this case; on the contrary, change of the line profile makes narrow *peaks* around 7 keV (figure 12). Such peaks were predicted in model A of Niedźwiecki & Miyakawa (2010); they showed that increase of fractional variability in the Fe-K energy band is produced especially in the low-inclination cases ($i \leq 40$ deg). In this case, change of the Fe-K spectral shape depending on h is larger than the flux variability, and the variability amplitude rather increases. This rms peak brings us a strong statement that the relativistic light bending model has to be largely modified.

The 2D transfer functions, the lag-frequency plot, and the lag-energy spectrum have similar tendency to those for $i = 60$ deg, with small differences (figures 13, 14, 15). The lag-frequency plots look very similar, and the Fe-K features in the lag-energy plots are sharper and less redshifted, which reflects the line profiles in the energy spectra.

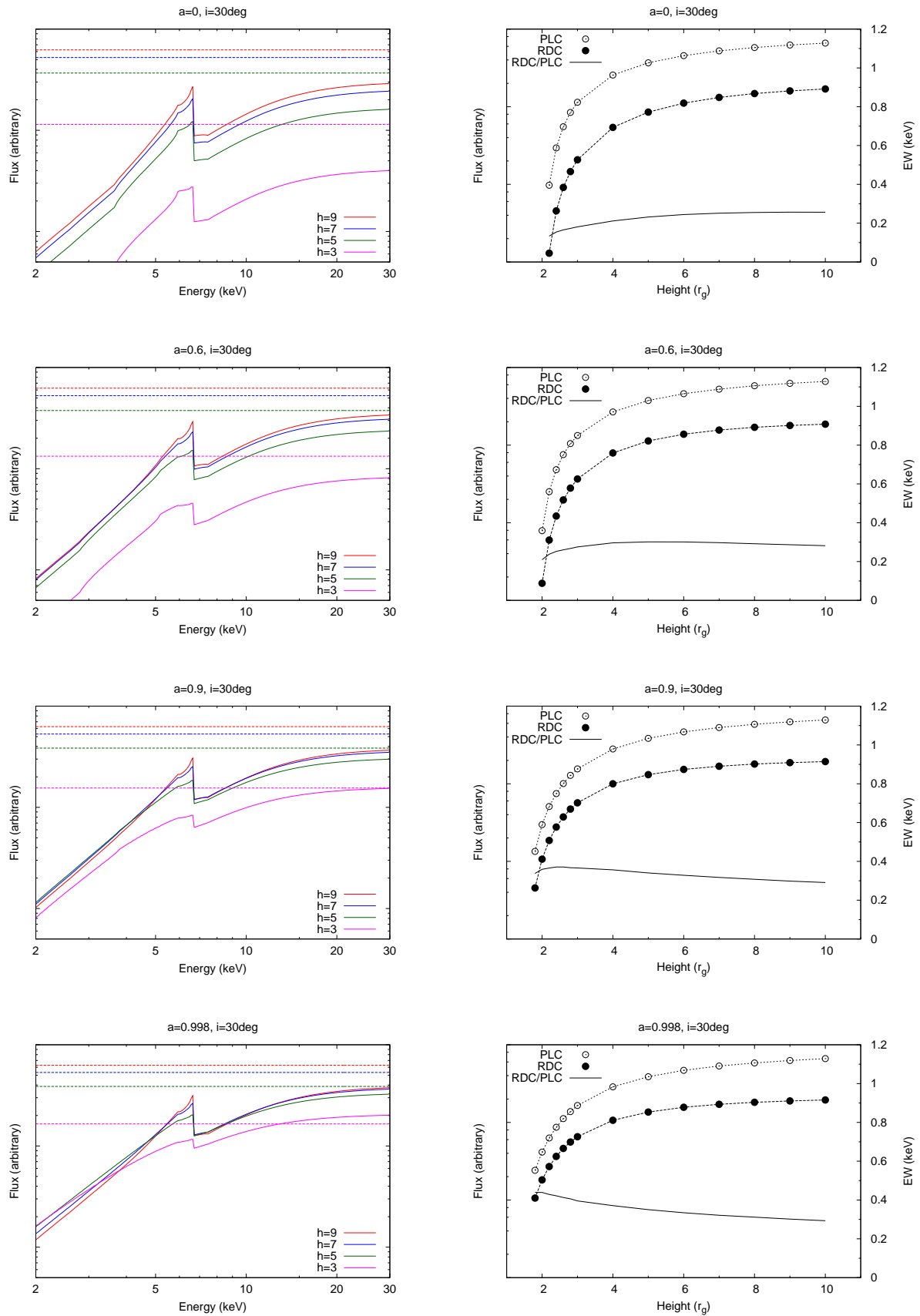


Fig. 11. Same as figure 2, but for $i = 30$ deg.

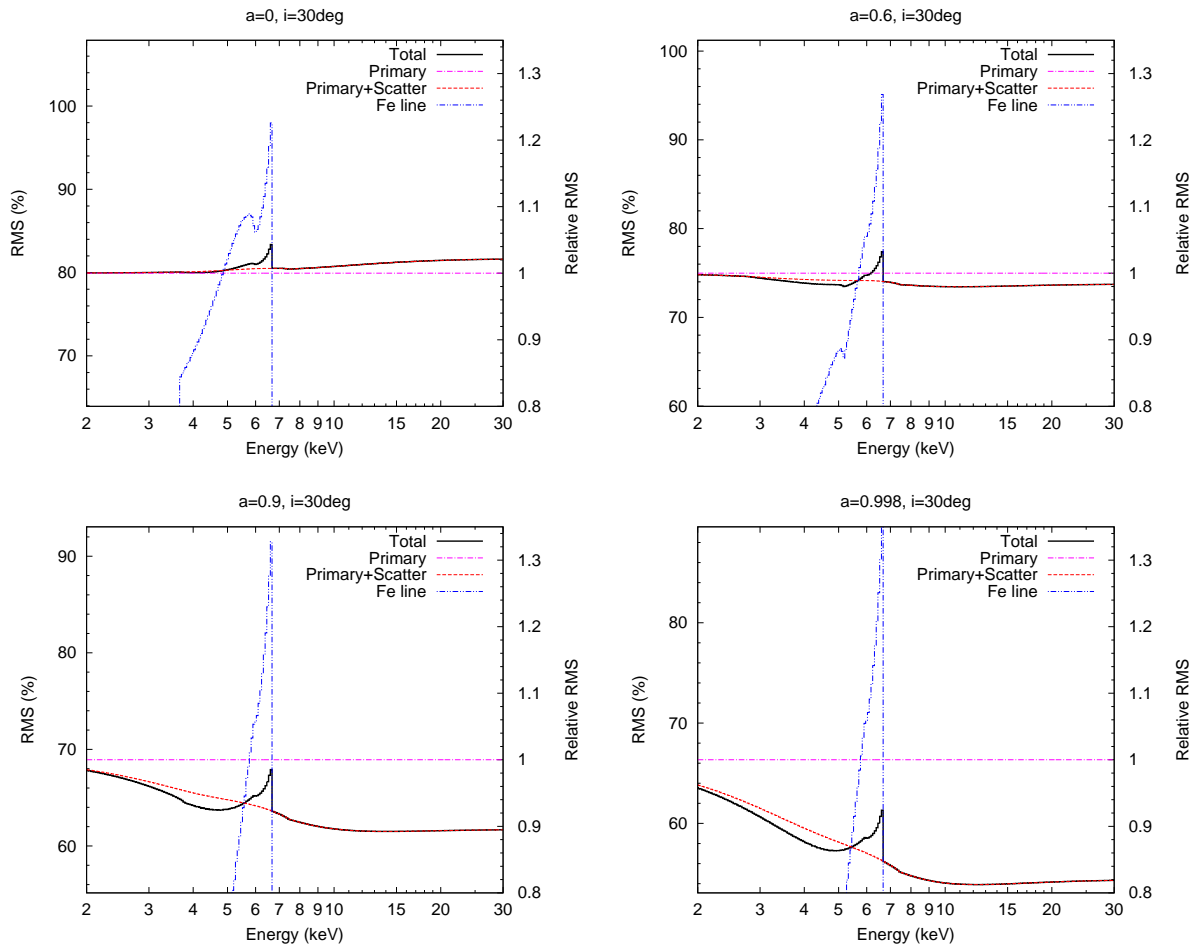


Fig. 12. Same as figure 3, but for $i = 30$ deg

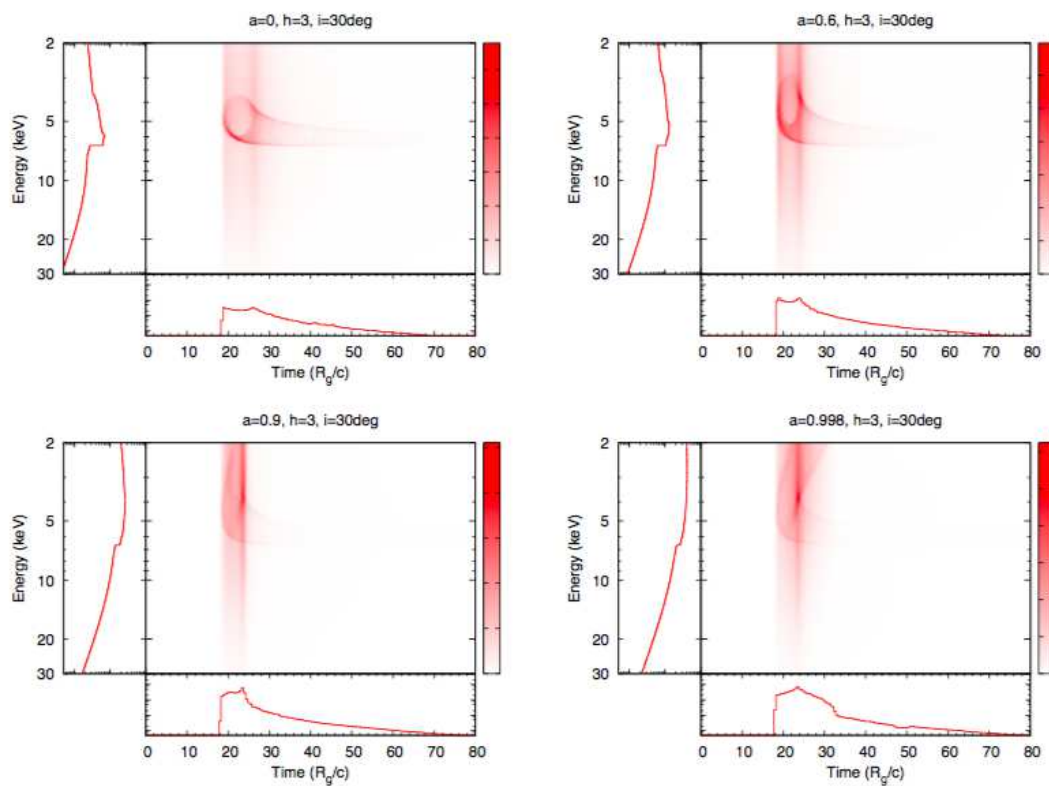


Fig. 13. Same as figure 4, but for $i = 30 \text{ deg}$

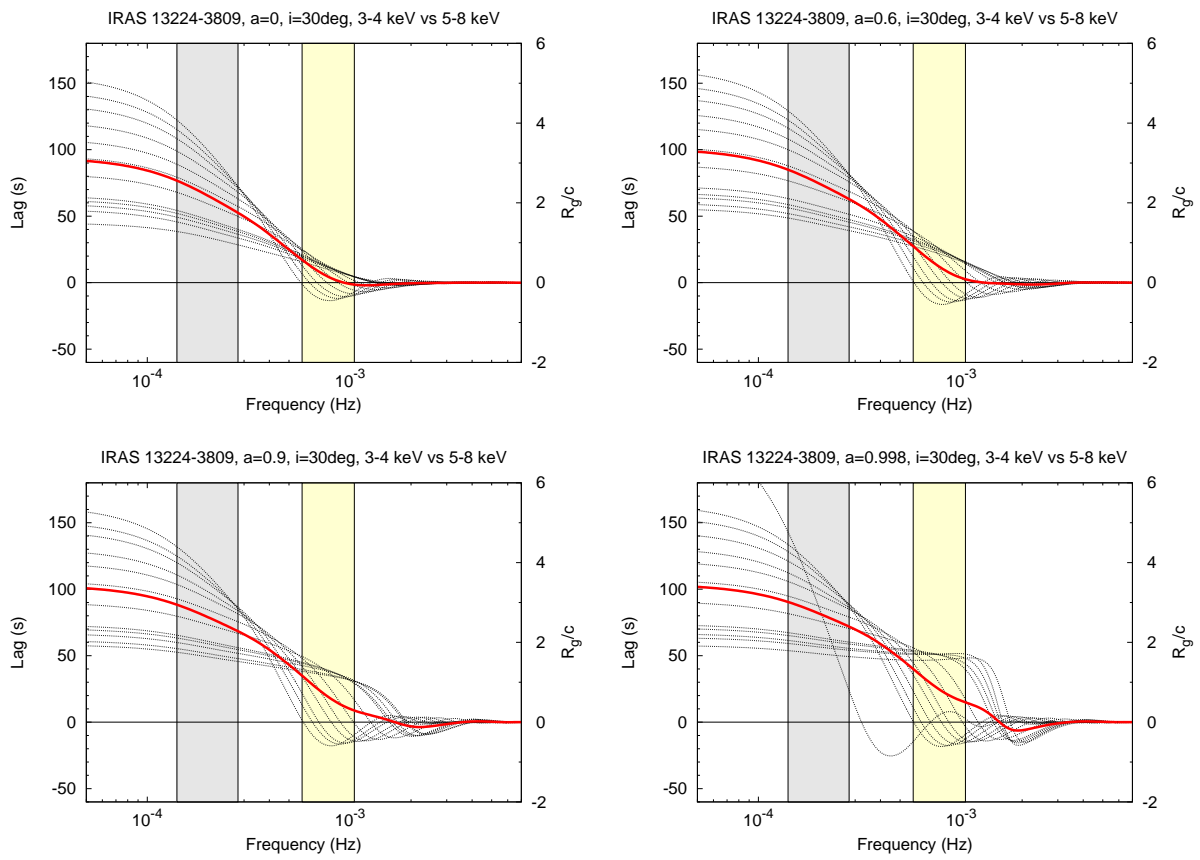


Fig. 14. Same as figure 5, but for $i = 30$ deg

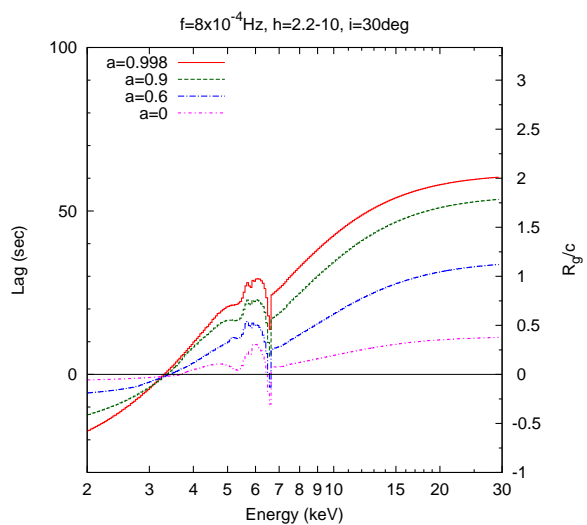


Fig. 15. Same as figure 6, but for $i = 30$ deg